JOURNAL OF AIRCRAFT
Vol. 48, No. 4, July–August 2011

Spurious Far-Field-Boundary Induced Drag in Two-Dimensional Flow Simulations

Daniel Destarac*
ONERA, 92190 Meudon, France

DOI: 10.2514/1.C031331

A hypothesis is made and evidence is given of a spurious far-field-boundary-induced drag component in two-dimensional flow numerical solutions, which is of a different nature from irreversible spurious drag. In the case of solutions to the Euler equations, analysis is carried out of its behavior with far-field boundary condition, lift coefficient, computational domain size, uniform grid refinement, far-field grid refinement, and flow regime (subcritical/transonic). Phenomenological breakdown of this drag component is derived through Taylor series expansion. Finally, the concept of far-field-boundary-induced drag is applied to the interpretation of some of the data contained in Vassberg and Jameson's results [Vassberg, J. C., and Jameson, A., "In Pursuit of Grid Convergence for Two-Dimensional Euler Solutions," *Journal of Aircraft*, Vol. 474, July–Aug. 2010, pp. 1152–1166]. Estimates of this component based on the aforementioned analysis are found to be coherent with, and to provide insight into, Vassberg and Jameson's results.

Nomenclature

$CD_{\text{fbi,sp}}$	=	spurious far-field-boundary-induced drag coefficient in two-dimensional flow
CD_i	=	induced (or vortex) drag coefficient
$CD_{\text{irr,sp}}$	=	spurious irreversible drag coefficient
CD_p	=	pressure-drag coefficient
CD_{vp}	=	viscous pressure-drag coefficient
CD_w	=	wave drag coefficient
CL_p	=	pressure lift coefficient
$\mathrm{d}L$	=	element of length
$\mathbf{i}$	=	unit vector in the freestream flow direction
L_{ref}	=	reference length for nondimensional coefficient definition
M	=	Mach number
$\mathbf{n}$	=	unit normal vector to the far-field boundary (pointing outward), $[n_x, n_y]^T$
p	=	static pressure
$\mathbf{q}$	=	velocity vector
R_{grid}	=	characteristic number of computational domain size
r	=	gas constant
r, θ	=	polar coordinates (no risk of confusion from the double definition of r)
U, V	=	velocity components in airfoil frame in two-dimensional flow
u, v	=	velocity components in the aerodynamic frame in two-dimensional flow
x, y	=	orthogonal coordinate system; x is freestream flow direction
α	=	angle of attack
γ	=	ratio of specific heats
ΔH	=	variation of stagnation enthalpy from its freestream value
Δs	=	variation of entropy from its freestream value
Δu	=	variation of u from its freestream value (u_∞)
Δv	=	variation of v from its freestream value (0)
ρ	=	density
∞	=	subscript for freestream state value

Received 30 November 2010; revision received 25 February 2011; accepted for publication 15 March 2011. Copyright © 2011 by the American Institute of Aeronautics and Astronautics, Inc. All rights reserved. Copies of this paper may be made for personal or internal use, on condition that the copier pay the $10.00 per-copy fee to the Copyright Clearance Center, Inc., 222 Rosewood Drive, Danvers, MA 01923; include the code 0021-8669/11 and $10.00 in correspondence with the CCC.

*Engineer, Applied Aerodynamics Department; daniel.destarac@onera.fr.

I. Introduction

THE object of this paper is to introduce the notion of spurious far-field-boundary-induced drag in two-dimensional flow, a drag component conspicuous with a certain type of far-field boundary condition. An attempt is made to apply it to some of Vassberg and Jameson's [1] results.

In a two-dimensional subcritical lifting flow around an airfoil, the linearized small-disturbance theory shows that velocity perturbations decrease as the inverse of the distance to the body in the far field (whereas they decrease much faster, as the inverse of the distance squared, in a three-dimensional flow). Therefore, violation of the physics of an unbounded flow through the application of a far-field boundary condition based on uniform freestream velocity will be stronger in two-dimensional flow than in three-dimensional flow. This observation, indisputable for solutions to the potential equation, may be extended to solutions to the Euler or Reynolds-averaged Navier–Stokes (RANS) equations.

Introduction into the boundary condition of a correction computed using a point-vortex representation of the airfoil (the circulation being coupled with the lift coefficient) is much more satisfactory. It has been shown that a boundary condition based on uniform freestream flow induces a strong dependency of the lift on the size of the computational domain, with insufficient size causing underestimated lift, and that this dependency is impressively reduced with the point-vortex correction [2,3].

In this paper the corresponding effect on pressure drag will be analyzed using the far-field approach to drag extraction.

II. Far-Field Boundary Condition

A common technique for treating subcritical far-field boundary conditions, when solving the Euler or RANS equations, consists of using characteristic relations associated with the normal to the boundary [4,5]. The basic way is to use nonperturbed velocity components in the Riemann invariants.

Early in the development of Euler solvers, it was found much more reliable to instead use velocity perturbations computed by modeling a lifting airfoil as a point vortex located at the quarter-chord of the camberline (a fair approximation to the moment center for subcritical flows) [3,6,7]. This approach is reliable in the sense that it almost cancels the otherwise strong influence of the computational domain size on the computed lift coefficient [2,3]. The vortex correction had been previously used for far-field potential in potential equation solvers [8].

The perturbation velocities computed using the linear small-disturbance compressible flow model (Prandtl–Glauert) are expressed in airfoil frame as

Table 1 Grid refinement levels

Level	Number of cells
1	256×32
2	512×64
3	1024×128

$$U - u_\infty \cos\alpha = \frac{1}{4\pi} u_\infty L_{\text{ref}} \sqrt{1 - M_\infty^2} \frac{\sin\theta}{(1 - M_\infty^2 \sin^2(\theta - \alpha))} \left(\frac{CL_p}{r}\right) \quad (1)$$

$$V - u_\infty \sin\alpha = -\frac{1}{4\pi} u_\infty L_{\text{ref}} \sqrt{1 - M_\infty^2} \frac{\cos\theta}{(1 - M_\infty^2 \sin^2(\theta - \alpha))} \left(\frac{CL_p}{r}\right) \quad (2)$$

where (r, θ) are the polar coordinates in an airfoil frame, whose pole is at the quarter-chord camberline. The last factor in Eqs. (1) and (2) shows that these perturbations decay in the far field as $1/r$ and vary proportionally to the lift coefficient.

III. Test Case

The airfoil used in this study is derived from the NACA0012 airfoil through trailing-edge extension, as described by Vassberg and Jameson [1]. It is symmetrical (zero lift at zero angle of attack) and the modification ensures zero trailing-edge thickness. The reference length used to define nondimensional aerodynamic coefficients is that of the original NACA0012 airfoil. The Euler equations are solved using a central-differencing scheme with Jameson's artificial dissipation, as implemented in the CANARI software [5,9]. Convergence is carried through to at least 10 orders of reduction of the residuals of all five equations.

C-type grids are generated with the Rizzi airfoil grid generator [10]. Unlike the grids of [1], they are not optimally orthogonal and the cells have aspect ratios far from 1 (for near-field refinement and far-field stretching). Dimensions of the three basic refinement levels used are given in Table 1. The grid of level n is derived from the grid of level $n + 1$ by eliminating every other node in both directions.

The size of the computational domain is a major parameter for this study. The domain size parameter R_{grid} is defined as the common number of chord lengths between the airfoil camberline and the C top and bottom, the leading edge and the upstream boundary, and the trailing edge and the downstream boundary. Computational domains of size in the range of $R_{\text{grid}} \in [10, 500]$ will be considered in this study.

IV. Spurious Far-Field-Boundary Induced Drag in Two-Dimensional Flow: Hypothesis

In the theoretical sections of this paper, the general case of a viscous flow modeled with the RANS equations will be considered, whereas in the sections on applications, only solutions to the Euler equations will be used. For three-dimensional numerical solutions, the near-field/far-field drag balance restricted to pressure components may be written as

$$CD_p = CD_{\text{vp}} + CD_w + CD_i + CD_{\text{irr,sp}} \quad (3)$$

Here, CD_p is the near-field pressure-drag coefficient. CD_{vp}, CD_w, and CD_i are, respectively, the far-field viscous pressure-drag coefficient, wave drag coefficient, and induced (or vortex) drag coefficient. $CD_{\text{irr,sp}}$ is the far-field spurious drag coefficient, in the sense of spurious drag as discussed in, e.g., [11–15]: drag generated through thermodynamically irreversible spurious processes. To make the distinction between this component and the object of this paper perfectly clear, far-field-boundary-induced drag, it will be called irreversible spurious drag and denoted as $CD_{\text{irr,sp}}$ instead of CD_{sp} as in the aforementioned references.

For two-dimensional numerical solutions, Eq. (3) should reduce to

$$CD_p = CD_{\text{vp}} + CD_w + CD_{\text{irr,sp}} \quad (4)$$

Basic numerical experience shows that the drag balance expressed by Eq. (4) is far from being satisfied numerically if the point-vortex correction is not used. We propose to introduce an additional term on the right-hand side of Eq. (4), so that the near-field/far-field drag balance becomes, in numerical two-dimensional flow,

$$CD_p = CD_{\text{vp}} + CD_w + CD_{\text{irr,sp}} + CD_{\text{fbi,sp}} \quad (5)$$

We will call this component *spurious far-field-boundary-induced drag* $CD_{\text{fbi,sp}}$, a denomination that will be justified in the following sections.

The far-field approach allows all drag components on the right-hand side of Eq. (5) to be integrated separately, including $CD_{\text{fbi,sp}}$ (as if it were CD_i in three-dimensional flow) as will be shown in the next section.

V. Spurious Far-Field-Boundary Induced Drag in Two-Dimensional Flow: Formulation

The formulation given in this section is valid for solutions to either the Euler equations or the RANS equations. It is restricted to two-dimensional flows.

In [16] a formula for induced drag in three-dimensional flow as a surface integral, not involving any viscous stress term, is derived from van der Vooren's original theory [14]. (Volume integrals are used in the original theory, surface integrals are used in the derived formulation, and the viscous stress term from the momentum equation, appearing in the induced-drag expression in [14], also appears instead in the viscous pressure and wave drag expressions in [16].)

In three-dimensional flow, spurious decay of vortical structures makes it a somewhat delicate matter to define the control volume for induced-drag integration. In two-dimensional flow, with this phenomenon being nonexistent, the whole computational domain may be taken without inconvenience. Formally extracting in two-dimensional flow what would be induced drag in three-dimensional flow will produce the reversible component of drag, whatever its origin.

As in [14], let us denote $\Delta\bar{u}$ as the scalar quantity,

$$\Delta\bar{u} = u[p = p_\infty, v = 0, \Delta H, \Delta s] - u_\infty \quad (6)$$

whose expression is

$$\Delta\bar{u} = u_\infty \sqrt{1 + 2\frac{\Delta H}{u_\infty^2} - \frac{2}{(\gamma - 1)M_\infty^2}\left[\left(e^{\frac{\Delta s}{r}}\right)^{\frac{\gamma-1}{\gamma}} - 1\right]} - u_\infty \quad (7)$$

Then the surface integral for the induced-drag coefficient in [16] becomes, in two-dimensional flow, the following line integral:

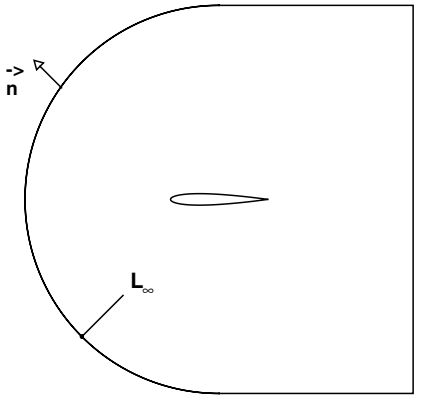

Fig. 1 Integration contour for spurious reversible far-field drag extraction in a two-dimensional flow around an airfoil.

$$CD_{\text{fbi,sp}} = \frac{2}{\rho_\infty u_\infty^2 L_{\text{ref}}} \int_{L_\infty} ([-\rho(u - u_\infty - \Delta\bar{u})\mathbf{q} - (p - p_\infty)\mathbf{i}].\mathbf{n})\, \mathrm{d}L \tag{8}$$

where L_∞ is the outer boundary of the planar computational domain, and the normal unit vector $\mathbf{n}$ is pointing outward, as illustrated in Fig. 1.

The problematic existence of $\Delta\bar{u}$, which requires that the quantity

$$1 + 2\frac{\Delta H}{u_\infty^2} - \frac{2}{(\gamma - 1)M_\infty^2}[(e^{\frac{\Delta s}{r}})^{\frac{\gamma-1}{\gamma}} - 1] \tag{9}$$

be positive, has been discussed by Méheut and Bailly [17]. This condition is fulfilled if and only if local stagnation pressure does not drop below freestream static pressure. This will very rarely happen at the outer boundary of the computational domain L_∞ involved in Eq. (8) and in none of the test cases considered in the present study.

VI. Spurious Far-Field-Boundary Induced Drag in Two-Dimensional Flow: Evidence

The numerical solutions used here to give evidence of far-field-boundary induced drag in two-dimensional flow are solutions to the Euler equations computed with the ONERA CANARI software [5] around the modified NACA0012 airfoil, with a freestream Mach number $M_\infty = 0.5$ and angles of attack $\alpha = 0$, 1.25, 2.5, 3.75, and 5°. The maximum angle of attack is chosen such that the flow is still entirely subcritical. Theoretical drag is equal to zero. The computational domain has a size parameter $R_{\text{grid}} = 150$ (as in [1]) and the grid refinement is of level 3 (see Table 1).

In the first series of computations considered here, the far-field condition is applied with the point-vortex correction switched off.

The equations solved are the Euler equations and the flow is entirely subcritical, and Eq. (5) thus reduces to

$$CD_p = CD_{\text{irr,sp}} + CD_{\text{fbi,sp}} \tag{10}$$

The three drag components appearing on either side of Eq. (10) are plotted against CL_p in Fig. 2. Far-field-boundary induced drag, negligible at zero lift, strongly increases with lift, following a law that will be discussed in the next section. Spurious irreversible drag weakly increases with lift or, rather, with the angle of attack or, better, with the pressure gradient at the leading edge.

Let us now perform the same series of computations with the point-vortex correction switched on. The results are plotted in Fig. 3. At zero lift the point vortex has zero intensity, and the solution computed with the correction switched on is hence identical to the one computed with the correction switched off. When lift increases, the increase of far-field-boundary induced drag is incomparably weaker with the correction switched on (Figs. 2 and 3 are at the same scale). Spurious irreversible drag is unaffected by the point-vortex correction.

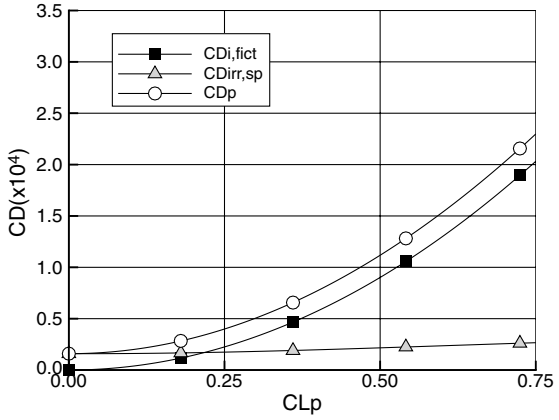

Fig. 2 Drag coefficient components vs pressure lift coefficient; far-field condition with point-vortex correction switched off ($M_\infty = 0.50$, $R_{\text{grid}} = 150$, and level-3 grid refinement).

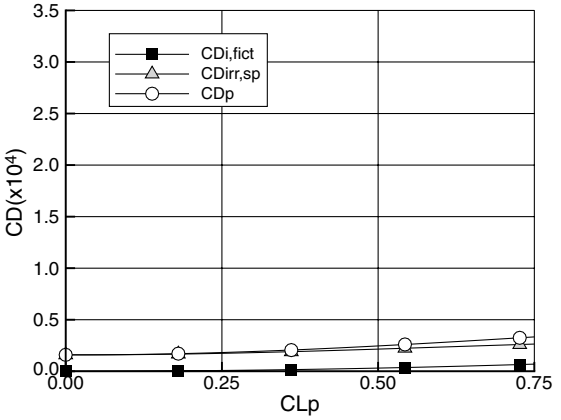

Fig. 3 Drag coefficient components vs pressure lift coefficient; far-field condition; point-vortex correction switched on ($M_\infty = 0.50$, $R_{\text{grid}} = 150$, and level-3 grid refinement).

At this stage, it has been shown that far-field-boundary induced drag exists in the two-dimensional solutions considered here and that the point-vortex correction almost suppresses it, but not quite. In the next section, this spurious component will be analyzed in detail.

VII. Spurious Far-Field-Boundary Induced Drag in Two-Dimensional Flow: Analysis

A. Lift Coefficient (Subcritical Flow)

The results presented in this section to discuss the effect of lift on far-field-boundary induced drag are again solutions to the Euler equations computed with the ONERA CANARI software [5] [9] around the modified NACA0012 airfoil with a freestream Mach number $M_\infty = 0.5$. They consist of two matrices of 25 computations:

$$[R_{\text{grid}} = 10, 20, 50, 150, 500]^T \otimes [\alpha = 0°, 1.25°, 2.5°, 3.75°, 5°]$$

All flows are entirely subcritical. Theoretical drag is equal to zero. One matrix is obtained with the point-vortex correction switched on, and the other is obtained with the point-vortex correction switched off. The grid refinement is of level 2 (512×64 cells). Both $(R_{\text{grid}}, \alpha)$ combinations considered by Vassberg and Jameson [1], ($R_{\text{grid}} = 150, \alpha = 0°$) and ($R_{\text{grid}} = 150, \alpha = 1.25°$), belong to these matrices.

In Figs. 2 and 3, the determination of the polynomial fit joining the symbols was left to the plotting software. Here, in Figs. 4–6, it is assumed that the laws $CD_{\text{fbi,sp}}(CL_p)$ are parabolas. The three constants of the parabolas are computed from the three smallest angles of attack, $\alpha = 0$, 1.25, and 2.5°, i.e., around the second angle of attack considered in [1]. Results for the two other angles of attack, $\alpha = 3.75$ and 5°, lie exactly on the parabolas determined from the first three, whether the point-vortex correction is used (Figs. 5 and 6) or not (Fig. 4). The level of far-field-boundary induced drag is strongly reduced by the point-vortex correction (the vertical scale in Figs. 4 and 5 is the same), but the behavior is alike parabolic.

B. Computational Domain Size (Subcritical Flow)

Let us take far-field-boundary induced drag interpolated for a given lift coefficient, $CL_p = 0.4$, along the parabolas of Figs. 4 and 5, and plot it against R_{grid}, the characteristic computational domain size number. Figure 7 shows that hyperbolas of the form $CD_{\text{fbi,sp}} = k/R_{\text{grid}}$ are fair approximations either with, or without, the point-vortex correction.

Far-field-boundary induced drag thus varies as CL_p^2/R_{grid}. If in the integrand of Eq. (8),

$$[-\rho(u - u_\infty - \Delta\bar{u})\mathbf{q} - (p - p_\infty)\mathbf{i}].\mathbf{n} \tag{11}$$

the leading-order terms follow $(\Delta u_{\text{vortex}})^2$ and/or $(\Delta u_{\text{vortex}}\Delta v_{\text{vortex}})$ and/or $(\Delta v_{\text{vortex}})^2$, where Δu_{vortex} and Δv_{vortex} are the velocity

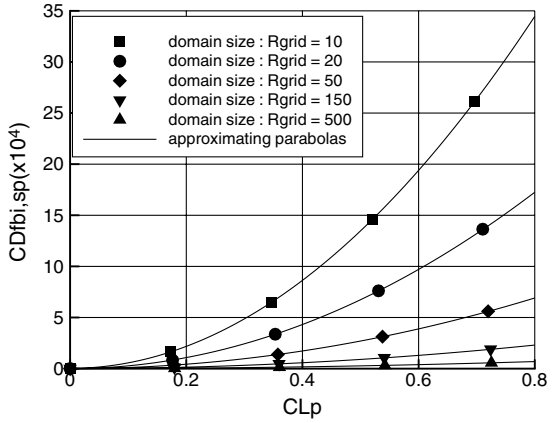

Fig. 4 Far-field-boundary induced-drag coefficient vs pressure lift coefficient; far-field condition with point-vortex correction switched off ($M_\infty = 0.50$ and level-2 grid refinement).

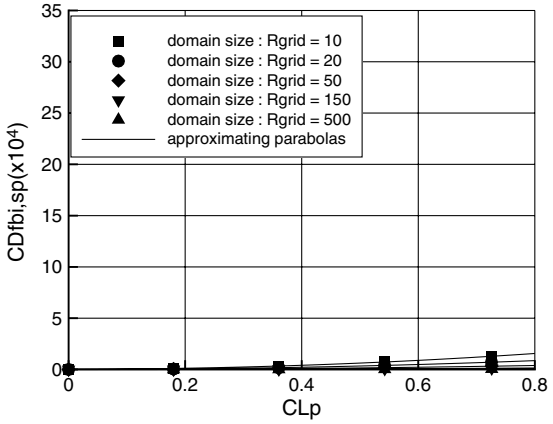

Fig. 5 Far-field-boundary induced-drag coefficient vs pressure lift coefficient; far-field condition with point-vortex correction switched on ($M_\infty = 0.50$ and level-2 grid refinement).

perturbations produced by the point vortex given in Eqs. (1) and (2), with the length of L_∞ varying proportionally to R_{grid}; this result is consistent with the linearized potential model.

C. Uniform Grid Refinement (Subcritical Flow)

When investigating a numerical phenomenon in computational fluid dynamics, an obvious and unavoidable step is the analysis of grid refinement effects. In this subsection, grid refinement is taken, as it usually is, as uniform: a coarser level being extracted from the finer one by eliminating every other node in each direction in the whole grid (see Table 1).

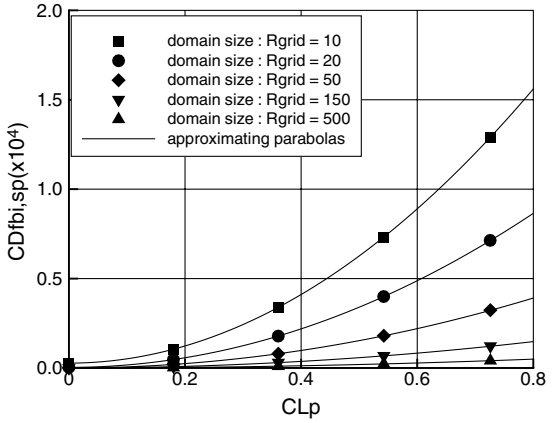

Fig. 6 Vertical blowup of Fig. 5.

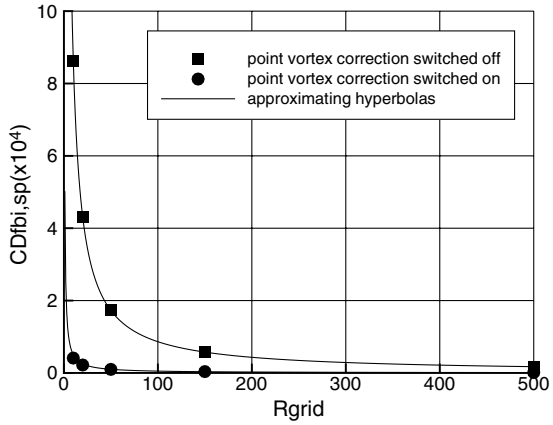

Fig. 7 Effect of the computational domain size on far-field-boundary induced drag at given lift ($CL_p = 0.4$, $M_\infty = 0.50$, and level-2 grid refinement).

The effect on the two spurious components of pressure drag, $CD_{\text{irr,sp}}$ and $CD_{\text{fbi,sp}}$, are plotted in Fig. 8 against CL_p with the point-vortex correction switched off and in Fig. 9 with the correction switched on. As expected, irreversible spurious drag decreases with grid refinement and tends toward zero, according to a likely order of scheme accuracy. It is not influenced by the far-field boundary condition (compare Figs. 8 and 9).

Without point-vortex correction, far-field-boundary induced drag is absolutely independent of the grid refinement (filled symbols are superimposed in Fig. 8), a rare feature in computational fluid dynamics for a nonphysical quantity. But with the point-vortex correction, this component does show some dependency on the grid refinement level.

At this point of the investigation, it is not difficult to anticipate, that this dependency is on the grid refinement close to the outer boundary and will be best analyzed by restricting refinement to some outer part of the grid. This is the object of the next subsection.

D. Outer-Grid Refinement (Subcritical Flow)

Here, grid visualization may be of some use. Figure 10 shows the grid of level 2, 512×64 cells, which in this subsection will be submitted to iterative refinement of an outer part of it. Following tradition, the i index runs along the airfoil from the lower downstream to the upper downstream boundary, and the j index runs away from the airfoil toward the outer C-shaped boundary.

The outer part of the grid considered is defined here as the rows or columns of two cells ending at the outer-boundary segments, i.e., if im and jm are the grid dimensions,

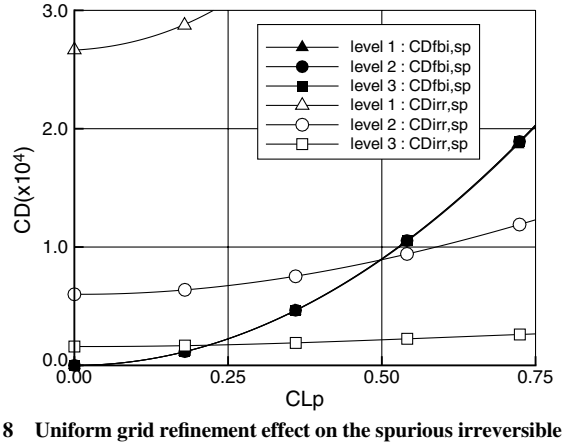

Fig. 8 Uniform grid refinement effect on the spurious irreversible and far-field-boundary induced-drag coefficients; far-field point-vortex correction switched off ($M_\infty = 0.50$ and $R_{\text{grid}} = 150$). Black symbols for the three refinement levels are almost superimposed.

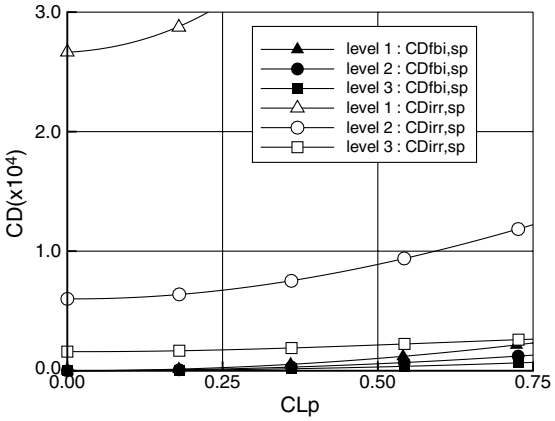

Fig. 9 Uniform grid refinement effect on the spurious irreversible and far-field-boundary induced-drag coefficients; far-field condition with point-vortex correction switched on ($M_\infty = 0.50$ and $R_{\text{grid}} = 150$).

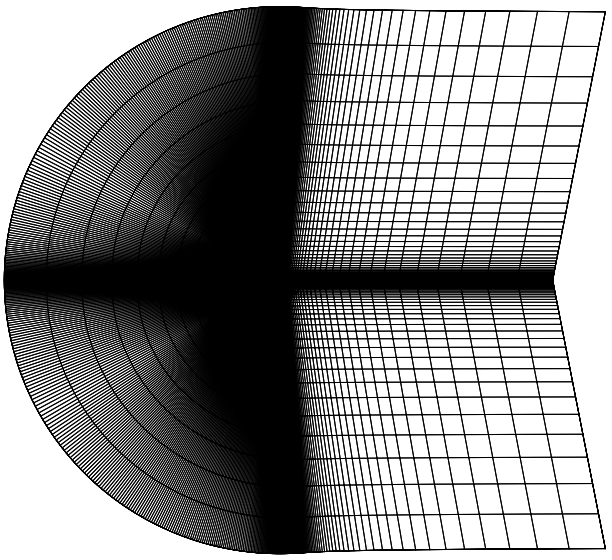

Fig. 10 Level-2 grid: 512 × 64 = [508 + (1 × 2) + (1 × 2)] × [62+ (1 × 2)] cells.

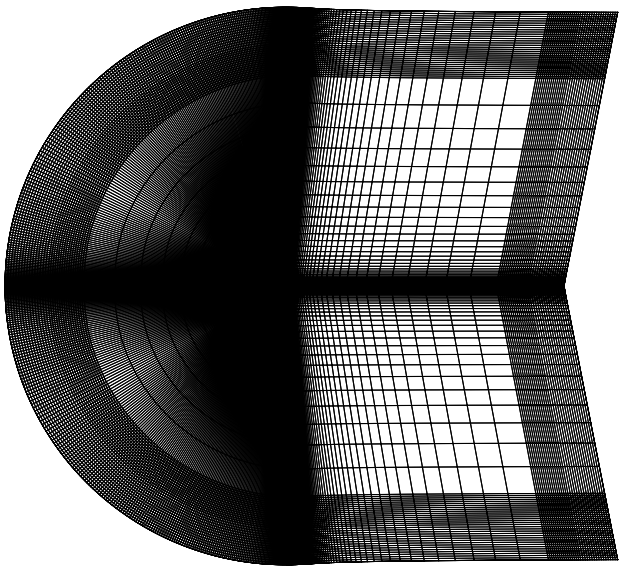

Fig. 11 Outer refinement of level-2 grid, iteration 4: 572 × 94 = [508 + (2^4 × 2) + (2^4 × 2)] × [62 + (2^4 × 2)] cells.

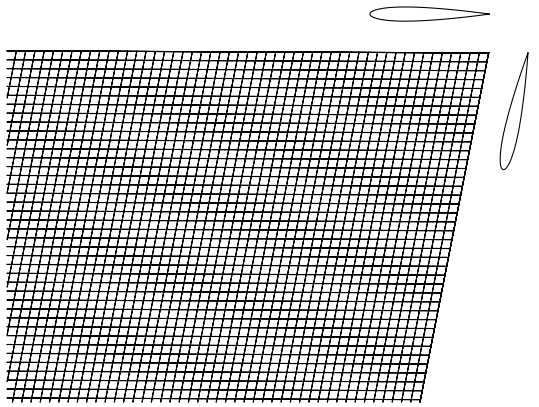

Fig. 12 Outer refinement of level-2 grid, iteration 8: enlargement of the upper-right corner with comparison of the cell size to the airfoil size.

$$[(1, 2 + 1) \times (1, jm)] \cup [(im - 2, im)) \times (1, jm)] \cup [(1, im) \times (jm - 2, jm)]$$

The corresponding inner part of the computational domain extends to about 115 chord lengths away from the airfoil.

In the outer part of the grid only, at each refinement iteration, cells are submitted to dichotomy in the direction pointing toward the boundary. (In the downstream upper and lower angles of the domain, dichotomy in both directions breaks down each cell into four cells instead of two.) At refinement iteration n, the grid thus numbers $[508 + 2 \times 2^n + 2 \times 2^n] \times [62 + 2 \times 2^n]$ cells.

The outer refinement procedure is illustrated in Fig. 11 (to be compared with Fig. 10), showing the grid obtained at iteration 4. Refinement was carried through to iteration 8. Figure 12 shows an enlargement of the upper-right corner of the grid obtained at iteration 8: the grid mesh-size length normal to the boundary is $\Delta\eta \simeq 0.08$ airfoil chord length.

The results for far-field-boundary induced drag are shown in Figs. 13 and 14. Here, the horizontal axis is a relative measure of the grid mesh size normal to the outer boundary. The level-2 grid corresponds to

$$\frac{\Delta\eta}{\Delta\eta(\text{level 2})} = 1$$

and refinement iteration 0. The point farthest to the left corresponds to

$$\frac{\Delta\eta}{\Delta\eta(\text{level 2})} = \frac{1}{256}$$

and refinement iteration 8.

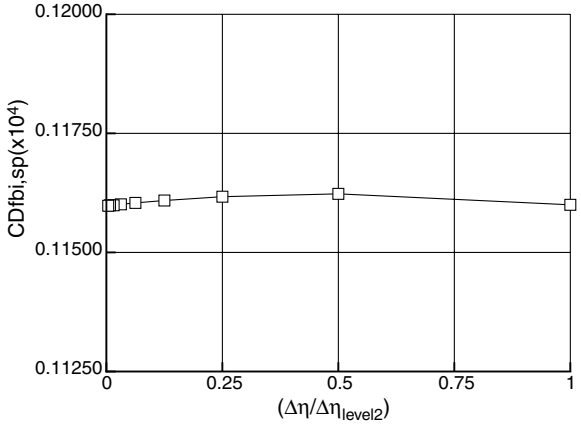

Fig. 13 Effect of outer-grid refinement on far-field-boundary induced drag; far-field condition with point-vortex correction switched off ($M_\infty = 0.50$, $\alpha = 1.25°$, $R_{\text{grid}} = 150$, and coarsest grid is level 2).

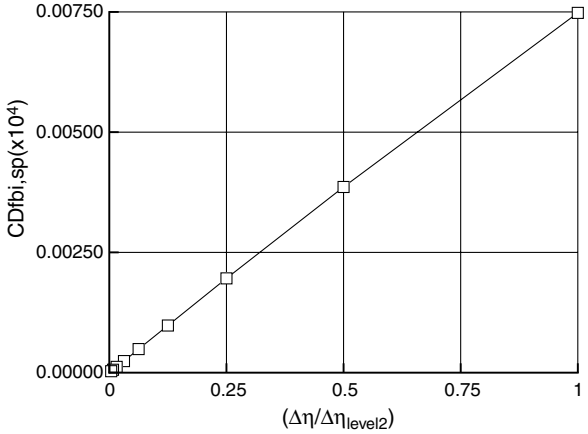

Fig. 14 Effect of outer-grid refinement on far-field-boundary induced drag; far-field condition with point-vortex correction switched on ($M_\infty = 0.50$, $\alpha = 1.25°$, $R_{\text{grid}} = 150$, and coarsest grid is level 2).

The vertical axes in Figs. 13 and 14 have identical spacing (0.0025 drag counts between two graduations). The contrast between the behavior of far-field-boundary induced drag with the point-vortex correction switched off and switched on is striking.

Without the correction, $CD_{\text{fbi,sp}}$ is of the order of one-tenth of a drag count (one drag count is equal to 10^{-4}) and is very weakly dependent on the outer-grid refinement level. This is in agreement with the results plotted in Fig. 8 (uniform grid refinement).

With the correction, $CD_{\text{fbi,sp}}$ tends toward zero, almost proportionally to the mesh spacing normal to the boundary.

Perturbation velocities induced by a vortex in small-disturbance linearized potential two-dimensional flow, decay in the far field as $1/r$ [Eqs. (1) and (2)]. The contrast between Figs. 13 and 14 may illustrate the fact that far-field grid refinement is important for accurately modeling a "dying" perturbation, whereas this is not so for modeling a "dead" perturbation (zero perturbation).

E. Transonic Flow

The vortex correction is valid under the hypothesis of the Prandtl–Glauert linear small-disturbance equation (compressible but entirely subcritical flow). It is thus not theoretically justified in transonic flow. Among the authors who have discussed this boundary condition, some (such as Rizzi [2]) chose to apply it only in its domain of validity (subcritical flow). Others (Pulliam and Steger [3]) pragmatically tested it in transonic flow and found its efficacy somewhat reduced but still good. Vassberg and Jameson's [1] transonic conditions for the modified NACA0012 airfoil are $M_\infty = 0.8$ with $\alpha = 0°$ and $M_\infty = 0.8$ with $\alpha = 1.25°$. The range of conditions considered in this subsection for far-field-boundary induced-drag analysis in transonic flow includes both these conditions: $M_\infty = 0.8$ with $\alpha = 0, 0.3125, 0.625, 0.9375, 1.25, 1.5625$, and 1.875 (uniform angle-of-attack step). These conditions imply from fairly strong to very strong shock waves.

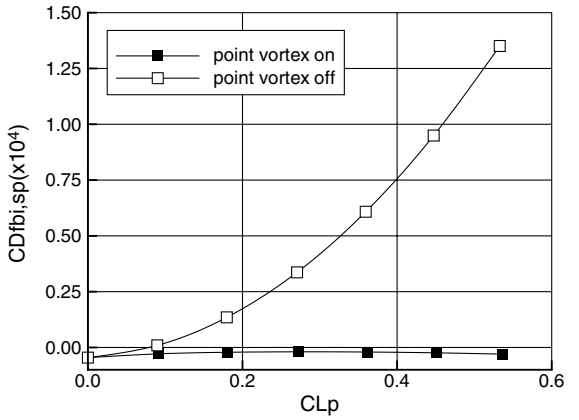

Fig. 15 Far-field-boundary induced-drag coefficient vs pressure lift coefficient in transonic flow ($M_\infty = 0.80$, $R_{\text{grid}} = 150$, and level-2 grid refinement).

The far-field-boundary induced-drag coefficient is plotted against the pressure lift coefficient in Fig. 15, with the point vortex switched off and switched on. Deviations from the subcritical flow behavior are obvious.

Without correction, far-field-boundary induced drag does increase with lift, but no parabola can match its behavior (polynomial fit is left to the plotting software here). At zero lift, neither its value (negative) nor its derivative relative to lift (positive) is zero.

With the correction on, far-field-boundary induced drag is much smaller, but negative and nonmonotonous with lift.

In subcritical flow, far-field-boundary induced drag has been found to be zero at zero lift. Such is not the case in transonic flow, as shown in Fig. 15. But if the grid is refined normal to the far-field boundary following the procedure described in the previous subsection, far-field-boundary induced drag tends toward zero (see Fig. 16, with computations point-vortex correction switched on). The local refinement requirement for vanishing drag is extremely severe, perhaps as fine as the requirement at the airfoil surface. The datum farthest to the left in Fig. 16 was obtained at local refinement iteration 8 (see Fig. 12). This singular effect in transonic flow is described here, not explained.

Well outside the range of validity of the Prandtl–Glauert linear small-disturbance equation, from which the point-vortex correction formulas (1) and (2) are derived, the behavior described in the previous subsections for subcritical flow is completely changed. This point will be discussed further in the next subsection through breakdown of far-field-boundary induced drag.

F. Breakdown

In the integrand of Eq. (8), p and ρ can be expressed as functions of u, v, Δs, and ΔH:

$$p = p_\infty e^{\left(-\frac{\Delta s}{r}\right)}\left[1 + \frac{(\gamma-1)M_\infty^2}{2}\left(1 - \frac{u^2+v^2}{u_\infty^2} + \frac{2\Delta H}{u_\infty^2}\right)\right]^{\left(\frac{\gamma}{\gamma-1}\right)} \quad (12)$$

$$\rho = \rho_\infty e^{\left(-\frac{\Delta s}{r}\right)}\left[1 + \frac{(\gamma-1)M_\infty^2}{2}\left(1 - \frac{u^2+v^2}{u_\infty^2} + \frac{2\Delta H}{u_\infty^2}\right)\right]^{\left(\frac{1}{\gamma-1}\right)} \quad (13)$$

If the following small-disturbance assumptions are valid along L_∞,

$$\frac{\Delta u}{u_\infty} \ll 1, \qquad \frac{\Delta v}{u_\infty} \ll 1, \qquad \frac{\Delta s}{r} \ll 1, \qquad \frac{\Delta H}{u_\infty^2} \ll 1 \quad (14)$$

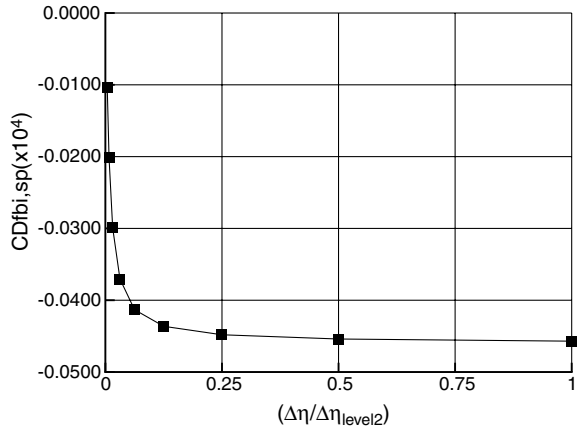

Fig. 16 Far-field-boundary induced drag at zero lift in transonic flow: effect of local grid refinement normal to the far-field boundary ($M_\infty = 0.80$, $\alpha = 0°$; $R_{\text{grid}} = 150$; coarsest grid: level 2; point-vortex correction switched on).

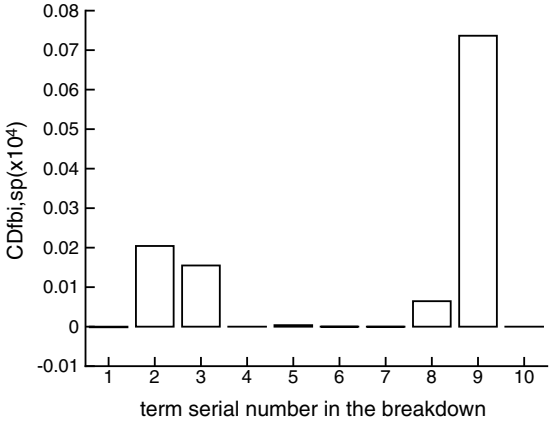

Fig. 17 Far-field-boundary induced-drag coefficient breakdown; far-field condition with point-vortex correction switched off ($M_\infty = 0.50$, $\alpha = 1.25°$, $R_{\text{grid}} = 150$, and level-2 grid refinement).

the nonzero first-order terms ($\Delta u/u_\infty$, $\Delta s/r$, and $\Delta H/u_\infty^2$) cancel out in the expansion of Eq. (8), which takes the form

$$
\begin{aligned}
CD_{\text{fbi,sp}} \simeq\ & +\kappa_1\left(\frac{\Delta u}{u_\infty}\right)^2 + \kappa_2\left(\frac{\Delta v}{u_\infty}\right)^2 + \kappa_3\left(\frac{\Delta u}{u_\infty}\right)\left(\frac{\Delta v}{u_\infty}\right) \\
& + \kappa_4\left(\frac{\Delta s}{r}\right)^2 + \kappa_5\left(\frac{\Delta H}{u_\infty^2}\right)^2 + \kappa_6\left(\frac{\Delta u}{u_\infty}\right)\left(\frac{\Delta s}{r}\right) \\
& + \kappa_7\left(\frac{\Delta v}{u_\infty}\right)\left(\frac{\Delta s}{r}\right) + \kappa_8\left(\frac{\Delta u}{u_\infty}\right)\left(\frac{\Delta H}{u_\infty^2}\right) + \kappa_9\left(\frac{\Delta v}{u_\infty}\right)\left(\frac{\Delta H}{u_\infty^2}\right) \\
& + \kappa_{10}\left(\frac{\Delta s}{r}\right)\left(\frac{\Delta H}{u_\infty^2}\right) \qquad (15)
\end{aligned}
$$

where $(\kappa_i)_{i=1,10}$ are nondimensional coefficients, depending on the freestream Mach number.

The 10-term breakdown is plotted in Fig. 17 (correction switched off) and Fig. 18 (correction switched on) for the subcritical case $M_\infty = 0.5$ and $\alpha = 1.25°$. The profile of the breakdown is quite different, depending on the far-field boundary condition used.

With the point-vortex correction, the dominant terms in the $CD_{\text{fbi,sp}}$ breakdown are two velocity terms, $\kappa_1(\Delta u/u_\infty)^2$ (squared velocity term) and $\kappa_3(\Delta u/u_\infty)(\Delta v/u_\infty)$ (crossed velocity term).

Without the correction, the dominant terms in Eq. (15) are $\kappa_2(\Delta v/u_\infty)^2$, $\kappa_3(\Delta u/u_\infty)(\Delta v/u_\infty)$, $\kappa_8(\Delta u/u_\infty)(\Delta H/u_\infty^2)$, and $\kappa_9(\Delta v/u_\infty)(\Delta H/u_\infty^2)$. The role played by $(\Delta H/u_\infty^2)$ in the latter case justifies plotting this quantity in the field: compare Fig. 19 (correction switched off) with Fig. 20 (correction switched on).

It is clear that without the correction the energy equation reacts to the boundary condition, producing a stagnation-enthalpy gradient.

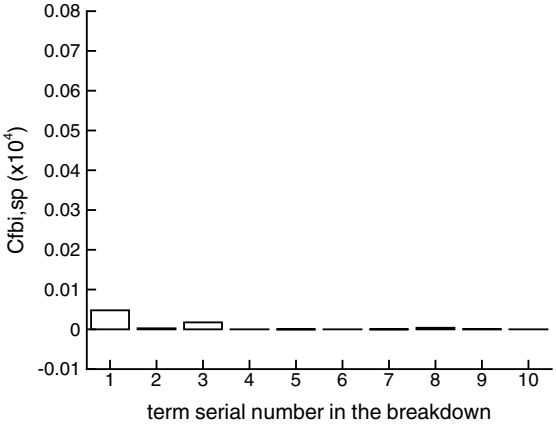

Fig. 18 Far-field-boundary induced-drag coefficient breakdown; far-field condition with point-vortex correction switched on ($M_\infty = 0.50$, $\alpha = 1.25°$, $R_{\text{grid}} = 150$, and level-2 grid refinement).

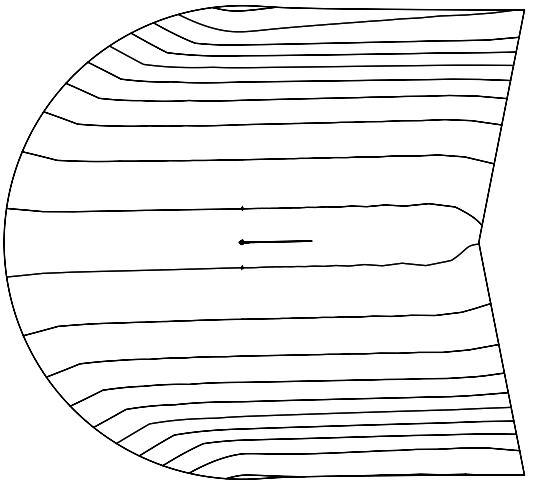

Fig. 19 Stagnation-enthalpy contours with point-vortex correction switched off; $\Delta H/u_\infty^2 = 10^{-5}$ between two contour lines; ($M_\infty = 0.50$, $\alpha = 1.25°$, $R_{\text{grid}} = 150$, and level-2 grid refinement).

(Note that the CANARI solver does not use enthalpy damping.) That this gradient is normal to the velocity is consistent with the continuity equation and with the energy equation in the steady flow Euler model,

$$\text{div}\,(\rho\mathbf{q}) = 0, \qquad \text{div}(\rho\Delta H\mathbf{q}) = 0 \qquad (16)$$

implies that

$$(\mathbf{q}.\mathbf{grad}\Delta H) = 0 \qquad (17)$$

but that this gradient is significantly different from zero is contrary to the physics of inviscid, non-heat-conducting, steady, two-dimensional flow in an infinite medium.

The 10-term breakdowns for the transonic case, $M_\infty = 0.8$ and $\alpha = 1.25°$, are plotted in Figs. 21 and 22.

In this case, the $\kappa_4(\Delta s/r)^2$, $\kappa_6(\Delta u/u_\infty)(\Delta s/r)$, and $\kappa_7(\Delta v/u_\infty)(\Delta s/r)$ terms are not negligible compared with the squared or crossed velocity and stagnation-enthalpy terms. Entropy variations, which are only spurious in the subcritical case, are predominantly physical in strongly transonic flow and of consequence in the far-field-boundary induced-drag breakdown [Eq. (15)]. This explains why the parabolic behavior of $CD_{\text{fbi,sp}}$ in subcritical flow no longer holds when strong shock waves are present. Analysis of gradual

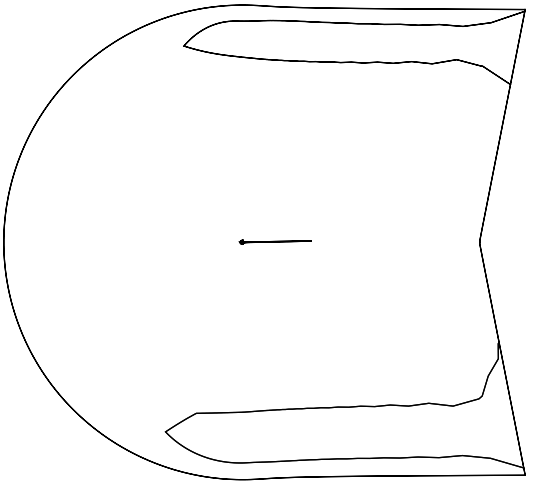

Fig. 20 Stagnation-enthalpy contours with point-vortex correction switched on; $\Delta H/u_\infty^2 = 10^{-5}$ between two contour lines; ($M_\infty = 0.50$, $\alpha = 1.25°$, $R_{\text{grid}} = 150$, and level-2 grid refinement).

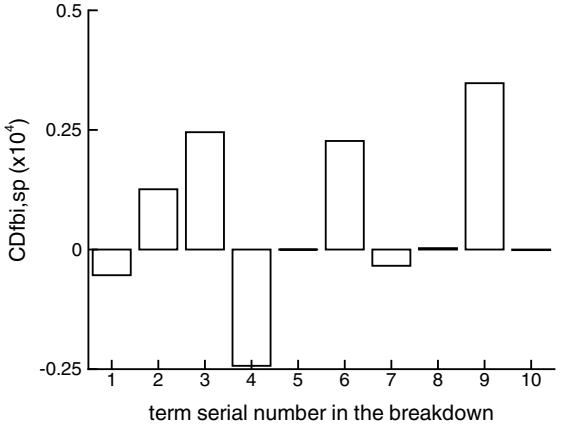

Fig. 21 Far-field-boundary induced-drag coefficient breakdown; far-field condition with point-vortex correction switched off ($M_\infty = 0.80$, $\alpha = 1.25°$, $R_{\text{grid}} = 150$, and level-2 grid refinement).

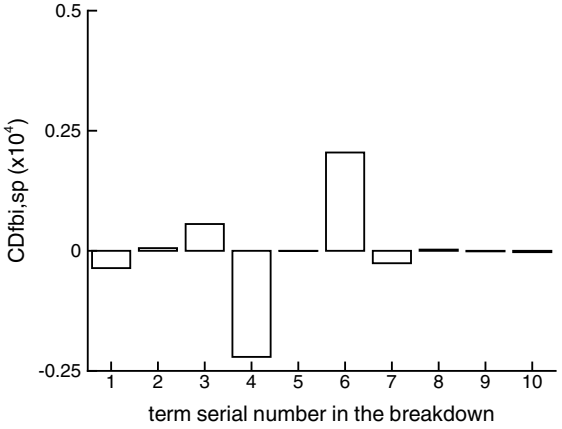

Fig. 22 Far-field-boundary induced-drag coefficient breakdown; far-field condition with point-vortex correction switched on ($M_\infty = 0.80$, $\alpha = 1.25°$, $R_{\text{grid}} = 150$, and level-2 grid refinement).

subcritical-to-transonic cases would probably show gradual deviation from the typical subcritical behavior.

VIII. Spurious Far-Field-Boundary Induced Drag in Two-Dimensional Flow: Synthesis

In two-dimensional flow, there exists a spurious far-field-boundary induced-drag component of a totally different nature from that of irreversible spurious drag. It is efficiently reduced, but not canceled, if a point-vortex correction is used in the far-field boundary condition.

In subcritical flow, it varies as the square of the lift coefficient and as the inverse of a characteristic number of the computational domain size. Its order of accuracy with respect to grid refinement normal to the far-field boundary is close to 1 with the point-vortex correction and near 0 without it.

In transonic flow, it obeys less-regular laws. A tremendous grid refinement requirement normal to the far-field boundary to obtain zero far-field-boundary induced drag at zero lift has been observed, but not explained.

IX. Application to Vassberg and Jameson's Results

A. Vassberg and Jameson's Test Case

In [1], grid convergence of two-dimensional Euler solutions is pursued for subcritical and transonic, nonlifting and lifting, flow conditions, with and without point-vortex correction applied to the far-field boundary condition. The modified NACA0012 considered in this reference has provided the datum for the study reported in the previous sections of the present paper. The grid strategy is completely different, with an O topology, ensuring optimal orthogonality, regularity, and cell aspect ratio of 1 through Kármán–Trefftz conformal transformation. Grid dimensions, identical in both directions, vary from 32×32 to 4096×4096, following a multigrid sequence (that has been called uniform refinement in the previous sections). The size of the computational domain in [1] is approached by $R_{\text{grid}} = 150$ in the present paper, a size that has purposely been uppermost considered in our study.

Of the three solvers employed, FLO82-HCUSP [4,18] uses the point-vortex correction, OVERFLOW [19] does not, and CFL3D [20] may either use it or not.

The order of accuracy of aerodynamic coefficients, denoted as p, is estimated from the three most refined levels (not necessarily the same for the three solvers). In subcritical flow, where pressure drag should be zero, the order of accuracy for this coefficient is also computed from the two most refined levels, assuming zero drag for infinite refinement (denoted as $\bar{p}$).

B. Two Different Behaviors of Drag in Grid Convergence

Only the pressure-drag coefficient for the subcritical lifting-flow case ($M_\infty = 0.5$ and $\alpha = 1.25°$) will be discussed here. Theoretical drag is equal to zero.

Two different behaviors, when tending toward zero cell size, are distinguished in [1]: that of the solutions computed without the point-vortex correction and that of the solutions computed with it. In the former case, pressure drag extrapolated to zero cell size using the empirical order of accuracy p is significantly (by Vassberg and Jameson's [1] standards, five digits below the drag count) different from zero. At the same time, $\bar{p}$ is significantly different, and smaller, than p.

In the latter case, with the point-vortex correction, pressure drag extrapolated to zero cell size is at least two orders of magnitude smaller, while $\bar{p}$ is now in fair agreement with p.

These results are transcribed from [1] in Tables 2 and 3. The number of significant digits has been preserved.

Let us add one column ($CD_{\text{fbi,sp}}$) and two lines (C grid, $R_{\text{grid}} = 150$, CANARI solver, correction switched off, and correction switched on) to Table 2. The extended table, Table 4, contains empty boxes: zero-cell-size extrapolation cannot be seriously attempted with the grids used for the CANARI computations (see Table 1), and far-field drag extraction has not been attempted in [1].

For $CD_{\text{fbi,sp}}$ extrapolation to zero cell size normal to the far-field boundary, a simple procedure has been followed: assume order of accuracy zero without correction and use the datum farthest to the left

Table 2 Pressure-drag values extrapolated to zero cell size in the case of $M_\infty = 0.5$ and $\alpha = 1.25°$[a]

Flow solver	Point-vortex correction	CD_p (zero cell size)
OVERFLOW	No	$+0.10030 \times 10^{-4}$
CFL3D	No	$+0.12221 \times 10^{-4}$
FLO82-HCUSP	Yes	$+0.00050 \times 10^{-4}$
CFL3D	Yes	-0.00134×10^{-4}

[a]Data transcribed from [1].

Table 3 Order of accuracy for pressure drag computed by two methods in the case of $M_\infty = 0.5$ and $\alpha = 1.25°$[a]

Flow solver	Point-vortex correction	p	$\bar{p}$
OVERFLOW	No	0.820	0.484
CFL3D	No	2.061	1.213
FLO82-HCUSP	Yes	1.805	1.932
CFL3D	Yes	2.060	2.077

[a]Data transcribed from [1].

Table 4 Pressure-drag and far-field-boundary induced-drag values extrapolated to zero cell size (whole field or far field) in the case of $M_\infty = 0.5$ and $\alpha = 1.25°$

Flow solver	Point-vortex correction	CD_p[a] (zero cell size)	$CD_{\text{fbi,sp}}$[b]
OVERFLOW	No	$+0.10030 \times 10^{-4}$	——
CFL3D	No	$+0.12221 \times 10^{-4}$	——
CANARI	No	——	$+0.11598 \times 10^{-4}$
FLO82-HCUSP	Yes	$+0.00050 \times 10^{-4}$	——
CFL3D	Yes	-0.00134×10^{-4}	——
CANARI	Yes	——	$+0.00000 \times 10^{-4}$

[a]Data transcribed from [1].
[b]Zero far-field cell size normal to the boundary.

in Fig. 13; assume order of accuracy one with the correction and use the two data farthest to the left in Fig. 14.

Without point-vortex correction, the agreement between the nonnegligible pressure-drag (near-field) values from [1] and the present far-field-boundary induced-drag (far-field) estimate is quite satisfactory, as though grid refinement and Richardson's extrapolation in [1] have indeed efficiently removed irreversible spurious drag, while leaving the other artificial component irreducible through grid refinement (order of accuracy near zero, see again Fig. 13). This component is of an entirely different nature (reversible) and is produced by a boundary condition, not through the inner cell scheme.

The strong effect (without point-vortex correction) of assuming ($\bar{p}$) or not assuming (p) zero pressure drag at zero cell size on the estimated order of accuracy (see Table 3) may be ascribed to the nonnegligible level of the far-field-boundary induced-drag component and to its approximately zero order of accuracy.

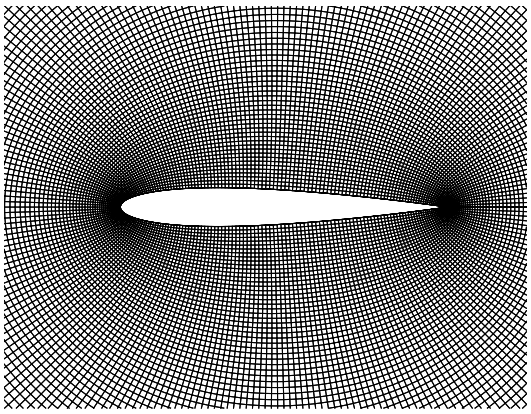

Fig. 23 Vassberg and Jameson's NACA0012 O grid [1]; dimensions of 257 × 257 nodes.

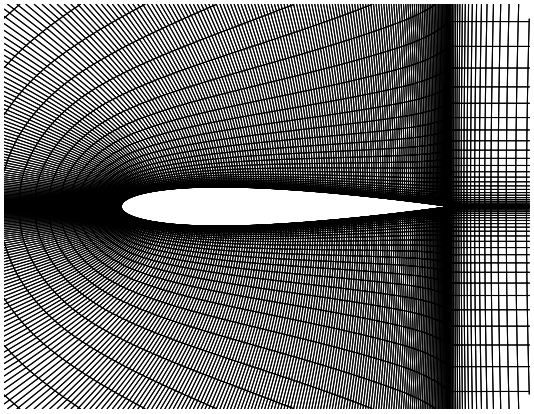

Fig. 24 NACA0012 C grid; Rizzi's grid generator [10]; dimensions of 513 × 65 nodes.

With point-vortex correction, all drag values are quite small. With the more common and relaxed standards of printing one-tenth of a drag count in the case of three-dimensional computations and 100th of a count in the case of two-dimensional computations, all of them would appear to be zero.

C. Spurious Far-Field-Boundary Induced Drag with Vassberg and Jameson'S Grids

When the present study was submitted to the authors of [1], they kindly made their grids available for confirmation or invalidation of

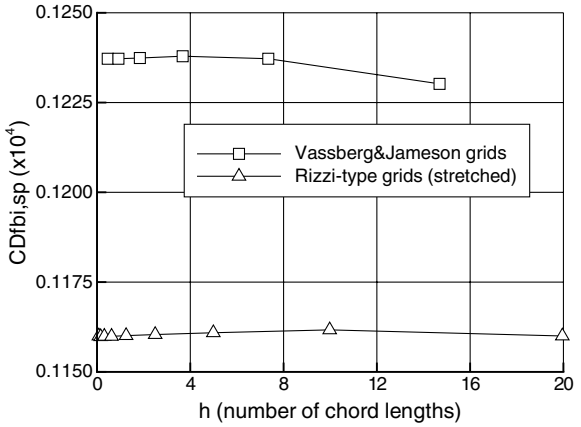

Fig. 25 Effect of outer-grid refinement on far-field-boundary induced drag for two types of grids; far-field condition with point-vortex correction switched off; h is the cell length normal to far-field boundary (NACA0012 airfoil, $M_\infty = 0.50$, $\alpha = 1.25°$, and $R_{\text{grid}} = 150$).

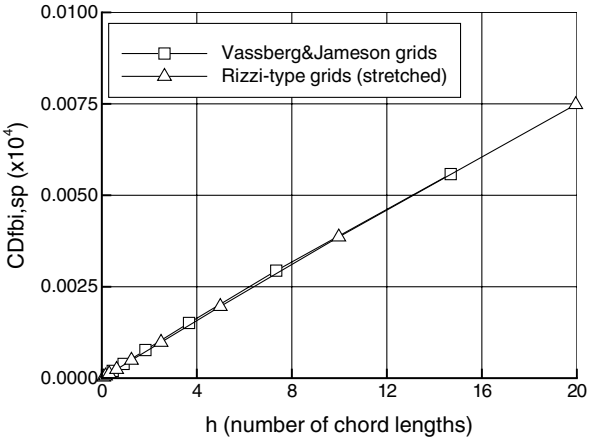

Fig. 26 Effect of outer-grid refinement on far-field-boundary induced drag for two types of grids; far-field condition with point-vortex correction switched on; h is the cell length normal to far-field boundary (NACA0012 airfoil, $M_\infty = 0.50$, $\alpha = 1.25°$, and $R_{\text{grid}} = 150$).

Table 5 Grid convergence of pressure and corrected pressure drag for computations without point-vortex correction ($CD_{p,\mathrm{corr}} = CD_p - CD_{\mathrm{fbi,sp}}$)[a]

	$CD_{\mathrm{fbi,sp}}(\times 10^4)$	$CD_p(\times 10^4)$		$CD_{p,\mathrm{corr}}(\times 10^4)$	
nc	CANARI + $ffd72$ (no vortex)	OVERFLOW	CFL3D (no vortex)	OVERFLOW	CFL3D (no vortex)
256	+0.12379	+1.18671	+6.49962	+1.06292	+6.37583
512	+0.12374	+0.68207	+1.63415	+0.55833	+1.51041
1024	+0.12372	+0.44071	+0.48451	+0.31699	+0.36079
2048	+0.12372	+0.29311	+0.20903	+0.16939	+0.07531
4096	+0.12372[b]	+0.20951	——	+0.08579	——
Continuum		**+0.10030**	**+0.12221**	**−0.02341**	**−0.01900**

[a]Pressure-drag data from [1]. Vassberg and Jameson's NACA0012 grids. Subsonic lifting case; $M_\infty = 0.50$ and $\alpha = 1.25°$.
[b]Extrapolated order 0.

Table 6 Grid convergence of pressure and corrected pressure drag for computations with point-vortex correction ($CD_{p,\mathrm{corr}} = CD_p - CD_{\mathrm{fbi,sp}}$)[a]

	$CD_{\mathrm{fbi,sp}}(\times 10^4)$	$CD_p(\times 10^4)$		$CD_{p,\mathrm{corr}}(\times 10^4)$	
nc	CANARI + $ffd72$ (vortex)	FLO82-HCUSP	CFL3D (vortex)	FLO82-HCUSP	CFL3D (vortex)
64	+0.00558	+19.74608	——	+19.74050	——
128	+0.00294	+2.98397	——	+2.98103	——
256	+0.00151	−0.11045	+6.38328	−0.11196	+6.38177
512	+0.00077	−0.15534	+1.51327	−0.15611	+1.51250
1024	+0.00039	−0.05301	+0.36185	−0.05340	+0.36146
2048	+0.00020	−0.01481	+0.08575	−0.01501	+0.08555
4096	+0.00010[b]	−0.00388	——	−0.00398	——
Continuum		+0.00050	−0.00134	+0.00047	−0.00144

[a]Pressure-drag data from Vassberg and Jameson's [1] NACA0012 grids. Subsonic lifting case is $M_\infty = 0.50$ and $\alpha = 1.25°$.
[b]Extrapolated order 1.

our observations. An example of these high-quality grids is shown in Fig. 23, to be compared with one of the grids considered in the previous sections (Fig. 24). Computations were carried out with the CANARI code, vortex-off and vortex-on, for six grid refinement levels: nc (equal number of cells in the two directions) equal to 64, 128, 256, 512, 1024, and 2049. The test case is the subsonic lifting case uses $M_\infty = 0.5$ and $\alpha = 1.25°$.

In Figs. 25 and 26, far-field-boundary induced drag is plotted against a common measure of the normal grid refinement to the outer boundary. The results obtained with Vassberg and Jameson's [1] grids are in good (vortex-off, Fig. 25) or excellent (vortex-on, Fig. 26) agreement with those presented in the previous sections. Near zero order of accuracy is obtained vortex-off, with a difference of less than 0.01 drag count between the two series of grids, and order one vortex-on, with a comforting identical slope.

At this point, it is tempting to subtract the far-field-boundary induced drag computed in the CANARI solutions from the pressure-drag values given in [1]. This is done in Table 5 for the solutions vortex-off and in Table 6 for the solutions vortex-on (`ffd72` is the name of the far-field drag-extraction postprocessor [13]). The CD_p column reproduces the data of [1], and the $CD_{p,\mathrm{corr}}$ column reproduces the corrected data. Of course, the correction changes almost nothing vortex-on, but modifies the continuum values vortex-off (shown in bold in Table 5).

In Figs. 27 and 28, drag is plotted against $1/nc$, where nc is the equal number of cells in the two directions, which is a simple conventional measure of grid refinement. It is apparent in these figures that, with far-field-boundary induced-drag correction, the two distinct families of solutions identified in [1] (vortex-on: white symbols; vortex-off: black symbols; for CANARI and CFL3D, white

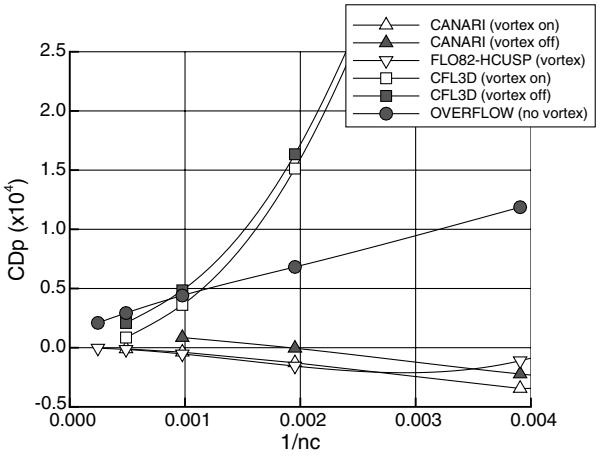

Fig. 27 Grid convergence of pressure drag (nc denotes the equal number of cells in the two directions). Vassberg and Jameson's NACA 0012 grids. Vortex correction: white symbols; no vortex correction: black symbols. All data except CANARI from [1] ($M_\infty = 0.50$, $\alpha = 1.25°$, and $R_{\mathrm{grid}} = 150$).

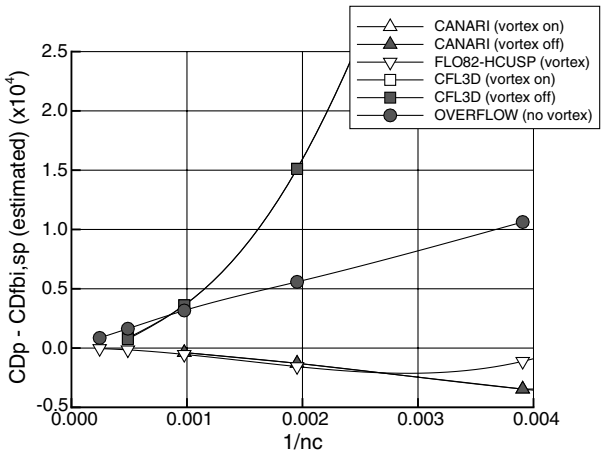

Fig. 28 Grid convergence of corrected pressure drag (nc denotes the equal number of cells in the two directions). Vassberg and Jameson's NACA0012 grids. Vortex correction: white symbols; no vortex correction: black symbols ($M_\infty = 0.50$, $\alpha = 1.25°$, and $R_{\mathrm{grid}} = 150$).

and black symbols are too close to be differentiated in Fig. 28) are no longer distinguishable when corrected. The scattering of continuum values is reduced and their average is brought nearer to zero. The fact that some corrected or uncorrected drag values reach zero from below with grid convergence in Figs. 27 and 28 and that some continuum drag values in Tables 5 and 6 are negative is extraneous to the matter of this paper and will be discussed in a separate Engineering Note.

X. Conclusions

Recently, the issue of aerodynamic performance accuracy attainable in two-dimensional flow with Euler solvers has been revisited through a more systematic approach and with considerably more computational means than when it was first addressed 25 years ago. Some of the copious and well-documented data produced inspired the present study, based on the far-field approach to drag extraction.

The hypothesis of a far-field-boundary induced-drag coefficient (spurious, nonphysical) existent in two-dimensional flow has been made. Its straightforward far-field formulation has been derived from van der Vooren's general three-dimensional theory. Evidence of its existence has been given. It has been shown to be strongly dependent on the type of far-field boundary condition, on the lift coefficient, and on the size of the computational domain.

Two types of far-field boundary condition have been considered: with and without the so called point-vortex correction. With point-vortex correction, influence of only local grid refinement normal to the far-field boundary has been observed. Without the correction, grid refinement, either uniform or local, has no influence on far-field-boundary induced drag, which is a rare feature in computational fluid dynamics for a nonphysical quantity.

This is explained by the fact that spurious far-field-boundary induced drag is of a totally different nature from that of the more frequently discussed irreversible spurious drag, which is known to be strongly dependent on grid refinement and artificial dissipation. Contrary to irreversible spurious drag, far-field-boundary induced drag is a reversible drag component determined by a boundary condition and is produced through a phenomenon involving no entropy variation along streamlines.

In subcritical flow, far-field-boundary induced drag obeys regular laws. It varies as the square of the lift and the inverse of a characteristic number of the computational domain size. With respect to local grid refinement normal to the far-field boundary, its order of accuracy is zero without the point-vortex correction and is one with it.

In transonic flow, i.e., outside the domain of validity of the theory on which the point-vortex correction is based, it follows less-regular laws. In particular, the tremendous local grid refinement requirement normal to the far-field boundary, found to be necessary to attain zero (instead of negative) far-field-boundary induced drag for zero lift in transonic flow, has not been explained.

In either subcritical or transonic flow, the point-vortex correction considerably reduces far-field-boundary induced drag. Pragmatism recommends its use even for transonic flow, despite the fact that the point-vortex correction is then being used outside its domain of theoretical validity. This paper has been written with a view to comment on some results of a paper in which only solutions to the Euler equations were discussed. Viscous flow has not been considered.

The issue of far-field-boundary induced drag in three-dimensional flow (where velocity perturbations vary differently in the far field) has also not been addressed. It has only been briefly touched upon in the literature. Work dedicated to this subject is in progress and its results will be submitted for publication.

The concept of far-field-boundary induced drag has been applied to the interpretation of some of the subcritical lifting-flow results. Estimates of this component based on the present analysis have been found to be coherent with, and to provide insight into, existing results.

Spurious drag is not a noble topic in aerodynamics. With spurious far-field-boundary induced drag, smallness of numbers is added to baseness of nature. This paper may be of some interest only to those whose pursuit is to dispatch the last drop of drag (spurious).

Acknowledgments

J. C. Vassberg and A. Jameson provided the author with the high-quality grids used and liberally authorized him to include data from their paper. V. Couaillier, the main author of the CANARI code, was always available for assistance. J. van der Vooren, the author of the far-field drag theory used in this study, kindly revised the manuscript. The phrase "far-field-boundary induced drag" is due to one of the reviewers of this paper.

References

[1] Vassberg, J. C., and Jameson, A., "In Pursuit of Grid Convergence for Two-Dimensional Euler Solutions," *Journal of Aircraft*, Vol. 47, No. 4, July–Aug. 2010, pp. 1152–1166. doi:10.2514/1.46737

[2] Rizzi, A., "Spurious Entropy Production and Very Accurate Solutions to the Euler Equations," *The Aeronautical Journal*, Vol. 89, No. 882, 1985, pp. 59–71.

[3] Pulliam, T. H., and Steger, J. L., "Recent Improvements in Efficiency, Accuracy and Convergence for Implicit Approximate Factorization Algorithms," AIAA Paper 85-0360, Jan. 1985.

[4] Jameson, A., "Solution of the Euler Equations for Two Dimensional Transonic Flow by a Multigrid Method," *Applied Mathematics and Computation*, Vol. 13, 1983, pp. 327–356. doi:10.1016/0096-3003(83)90019-X

[5] Couaillier, V., "Numerical Simulation of Separated Turbulent Flows Based on the Solution of RANS/Low Reynolds Two-Equation Model," 37th Aerospace Science Meeting and Exhibit, AIAA Paper 99-154, Reno, NV, 11–14 Jan. 1999.

[6] Salas, M. D., Jameson, A., and Melnik, R. E., "A Comparative Study of the Nonuniqueness Problem of the Potential Equation," AIAA 6th Computational Fluid Dynamics Conference, AIAA Paper 83-1888, Danvers, MA, July 1983.

[7] Thomas, J. L., and Salas, M. D., "Far-Field Boundary Conditions for Transonic Lifting Solutions to the Euler Equations," *AIAA Journal*, Vol. 24, No. 7, July 1986, pp. 1074–1080. doi:10.2514/3.9394

[8] Jameson, A., "Acceleration of Transonic Potential Flow Calculations on Arbitrary Meshes by the Multiple Grid Method," Fourth AIAA Computational Fluid Dynamics Conference, AIAA Paper 79-1458, July 1979.

[9] Couaillier, V., and Delbos, M., "Accurate Boundary Conditions with Classical and Higher Order CFD Methods," *RTO Applied Vehicle Technology Panel Symposium*, RTO MP-AVT-147, NATO Research and Technology Org., Paper 29, 3–6 Dec. 2007.

[10] Rizzi, A., "Computational Mesh for Transonic Airfoils," *Numerical Methods for the Computation of Inviscid Transonic Flow*, edited by A. Rizzi, and H. Viviand, Vieweg, Braunschweig, Germany, 1981.

[11] Destarac, D., "Far-Field Drag in Transonic Potential Flow: Analysis and Optimisation," *Proceedings of the 1993 European Forum, Recent Developments and Applications in Aeronautical CFD*, The Royal Aeronautical Society, Bristol, England, U.K., Sept. 1993.

[12] Tognaccini, R., "Methods for Drag Decomposition, Thrust-Drag Bookkeeping from, C. F.D. Calculations," *CFD-Based Aircraft Drag Prediction and Reduction*, VKI Lecture Series 2003, von Karman Inst. for Fluid Dynamics, Rhode-St-Genèse, Belgium, 2003.

[13] Destarac, D., "Far-Field/Near-Field Drag Balance and Applications of Drag Extraction in CFD," *CFD-Based Aircraft Drag Prediction and Reduction*, VKI Lecture Series 2003, von Karman Inst. for Fluid Dynamics, Rhode-St-Genèse, Belgium, 2003.

[14] Van der Vooren, J., and Destarac, D., "Drag/Thrust Analysis of Jet-Propelled Transonic Transport Aircraft: Definition of Physical Drag Components," *Aerospace Science and Technology*, Vol. 8, Sept. 2004, pp. 545–556. doi:10.1016/j.ast.2004.03.004

[15] Esquieu, S., "Reliable Drag Extraction from Numerical Solutions: Elimination of Spurious Drag," AVT Symposium RTO MP-AVT-147, Paper 42, Athens, Greece, 3–6 Dec. 2007.

[16] Destarac, D., "Drag Extraction from Numerical Solutions to the Equations of Fluid Dynamics: The Far-Field 'Philosophy'," *43ème Colloque d'Aérodynamique Appliquée de la 3AF*, Maîtrise de la Traînée et de l'Impact sur l'Environnement, Poitiers, France, 10–12 March 2008.

[17] Méheut, M., and Bailly, D., "Drag Breakdown Methods from Wake Measurements," *AIAA Journal*, Vol. 46, No. 4, April 2008, pp. 847–862.
doi:10.2514/1.29051

[18] Jameson, A., "Artificial Diffusion, Upwind Biasing, Limiters and their Effect on Accuracy and Multigrid Convergence in Transonic and Hypersonic Flow," AIAA 11th Computational Fluid Dynamics Conference, AIAA Paper 93-3359, Orlando, FL, July 1993.

[19] Nichols, R. H., and Buning, P. G., "User's Manual for OVERFLOW 2.1," Univ. of Alabama, and NASA, Aug. 2008.

[20] Krist, S. L., Biedron, R. T., and Rumsey, C. L., "CFL3D User's Manual, Ver. 5.0," NASA TM 1998-208444, June 1998.